Chapter 2

Details of experimental procedures

Abstract

In this chapter, the general insights into the experimental procedures followed to conduct the material characterization and test the photocatalytic activity regarding MB dye degradation with prepared photocatalysts' samples. The basic description of the experimental procedures will provide a better understanding of the experimental details discussed in subsequent chapters pertaining to specific photocatalysts, in lab-scale photochemical reactor.

2.1 Introduction

The desired performance of the photocatalyst in lab-scale testing supported by their favourable physicochemical characteristics analysed from various characterizations is indeed the first and foremost step towards putting the new and improved photocatalytic formulations for large-scale applications. Hence, the focus is always on adjusting the experimental conditions in such a way that the intrinsic activity of the catalytic formulations can be measured effectively without masking the results due to mass and energy transfer constraints. Hence, general insights into state-of-the-art methods and means used for the testing and material characterization of the prepared photocatalysts will be given in this chapter to provide a fair idea about the experiments performed.

2.2 Characterization Techniques:

The information on the structure of the catalysts provides insight into the relation between the parameters of catalysts preparation and the performance of the catalyst. Checking and understanding the critical features of a photocatalyst's structure is essential for ensuring quality standards, using information from past experiences. Knowing more about the catalyst helps us to improve the processes in which it is used and how the catalysts are prepared. Various Characterization techniques like Fourier Transform Infrared Spectrum (FTIR), X-ray diffraction (XRD) analysis, X-ray photoelectron spectroscopy (XPS), Scanning electron microscopy (SEM), Diffuse-Reflectance spectroscopy (DRS) and Transmission electron microscope (TEM) were used and summarized in Table 2.1.

Table 2.1 Techniques used for characterization of catalyst

S. No.	Instrument	Application
1.	X-ray diffraction (XRD)	Crystal structure- phase identification and crystallite size
2.	Diffuse reflectance spectroscopy (DRS)	Band gap energy
3.	X-ray photoelectron spectroscopy (XPS)	Element composition and oxidation state of elements
4.	Transmission electron microscope (TEM)	Imaging and particle size
5.	Scanning electron microscopy (SEM)	Morphology analysis
6.	Fourier transform infrared spectroscopy (FTIR)	Chemical bond information

2.2.1 FTIR and XPS analysis

FTIR and XPS were used for spectral analysis of the prepared photocatalysts samples.

2.2.1.1 FTIR spectrometer [1], [2]

In materials analysis, Infrared spectroscopy has long been a reliable method. The spectrum generated through infrared spectroscopy serves as a distinctive signature for a sample, displaying absorption peaks that correspond to vibrational frequencies between atomic bonds in the material. Since each material possesses a unique integration of atoms, the resulting infrared spectrum is distinct, making it a powerful tool for identifying different materials positively through qualitative analysis. Additionally, the amplitude of the peaks in the spectrum directly reflects the present quantity of the material. With the aid of modern software algorithms, infrared spectroscopy is adept at qualitative analysis and proves to be an excellent tool for quantitative analysis. It enables the identification of unknown materials and provides insights into the quality and consistency of a given sample.

2.2.1.2 Principle of FTIR:

FTIR utilizes a single optical component known as an interferometer. These interferometers usually incorporate a beam splitter that divides the incoming infrared beam into two optical beams. One of these beams reflects off a stationary flat mirror, while the other reflects off a flat mirror mounted on a mechanism that allows it to move a short distance (typically a few millimeters) away from the beam splitter. The two beams, each reflecting off their respective mirrors, reunite when they meet back at the beam splitter. The resulting signal, known as an interferogram, is formed by the interference of these two beams. This unique signal is characterized by the fact that each data point, determined by the position of the moving mirror, contains information about every infrared frequency. The FTIR analysis was done by KBr pellet technique using the Nicholet 5700 (Thermo Electron, Walthem, MA, USA) FTIR spectrophotometer. The infrared spectra were recorded at room temperature for the samples under investigation.

2.2.1.3 X-ray photoelectron spectroscopy (XPS)

XPS, or X-ray Photoelectron Spectroscopy, is a quantitative spectroscopic method designed to assess various aspects of a material's surface. It provides valuable insights into the elemental composition, empirical formula of pure substances, chemical and electronic states of the constituent elements, and surface contaminants. Furthermore, XPS enables the examination of the uniformity of elemental composition across the top surface of the material.

2.2.1.4 Principle of XPS:

This technique employs X-rays to displace electrons from inner-shell orbitals, constituting an electron spectroscopic method. The kinetic energy (E_k) of these photoelectrons is calculated based on the energy of the X-ray radiation (hν) and the electron binding energy (E_b), as outlined by the provided equation (2.1)

$$E_k = \mathrm{h\nu} - E_b \qquad (2.1)$$

The experimentally measured energies of the photoelectrons are given by equation (2.2).

$$E_k = \mathrm{h\nu} - E_b - E_w \qquad (2.2)$$

Where E_w is the work function of the spectrometer.

X-ray Photoelectron Spectroscopy (XPS) relies on the chemical environment of an atom to influence its electron binding energies, making it a valuable tool for determining the oxidation state and ligands of atoms. This technique is especially effective for examining the surfaces of solid materials, as the ejected electrons can only escape from a depth of approximately 3 nm or less. The XPS analysis was done using an Amicus spectrometer with Mg Kα X-ray radiation. The spectrometer operated at a voltage of 15 kV and a current of 12 mA during standard analysis, maintaining a pressure below 10^{-5} Pa in the analysis chamber. The binding energy scale was calibrated using the main C 1s line of adventitious impurities at 284.7 eV, introducing uncertainty in peak positions of ±0.2 eV

2.2.2 Scanning Electron Microscopy (SEM) [3], [4]

Morphological characterization was carried out using scanning electron microscopy (SEM), a technique employed to evaluate powders' average aggregate size and microstructures. SEM analysis is labeled as "non-destructive," indicating that the X-rays generated by electron interactions do not lead to any volume loss in the sample. Consequently, it is feasible to analyze the same materials repeatedly. Topographical images in SEM are generated from back-scattered primary or low-energy secondary electrons, with the highest resolution reaching around 2-5 nm. While many routine studies find satisfaction with lower resolution, leveraging the benefits of image interpretation and exceptional depth of field provides a comprehensive view of the specimen. In the case of non-crystalline catalysts, SEM is particularly valuable for examining the distribution and sizes of mesopores.

2.2.2.1 Principle of SEM

In SEM, electrons released from the electron gun are precisely focused onto a small spot, typically 50-100 Å in diameter, on the sample's surface. Electron beams accelerated through a voltage ranging between 1 and 50 kV are commonly utilized for various purposes. These accelerated electrons possess substantial kinetic energy, dissipated as diverse signals resulting from interactions between electrons and the sample when the incident electrons decelerate within the solid material. These signals include secondary electrons (producing SEM images), back-scattered electrons (BSE), diffracted back-scattered electrons (EBSD, used for determining crystal structures), photons (characteristic X-rays employed for elemental analysis and continuum X-rays), visible light, and heat.

Secondary electrons and back-scattered electrons are frequently employed for imaging samples. Secondary electrons are most advantageous for revealing morphology and topography, whereas back-scattered electrons are particularly effective in illustrating composition contrasts in multiphase samples, facilitating rapid phase discrimination.

2.2.3 Transmission Electron Microscopy (TEM) [5]

TEM is a technique that allows researchers to obtain high-resolution images of nanoscale samples and helpful information on material structural features. TEM is used to determine the crystal size and morphology of the material. This method involves using a beam of electrons that passes through an extremely thin sample, interacting with it along the way.

The interaction of these electrons with the specimen creates an image, which is then magnified and directed onto a visualizing tool, like a fluorescent screen or photographic film. Additionally, TEM analysis generates a Selected Area Electron Diffraction (SAED) image for the examined photocatalysts, aiding in identifying their lattice fringes. It's important to note that TEMs can provide much higher-resolution images than optical microscopes. In present study, TEM analyses were carried out using a model 20 G2 (Tecnai, FEI, USA) microscope.

2.2.4 X-Ray Diffraction analysis [6]

X-ray diffraction is the most extensively employed and unambiguous method for accurately determining the positions of atoms across a diverse range of materials, spanning fluids and powders to impeccably formed crystals. This non-destructive technique is widely utilized for characterizing crystalline materials, offering valuable insights into their structure. X-ray diffraction provides comprehensive information about various aspects, including the material's phases, preferred crystal orientation, and additional structural parameters such as lattice parameters, crystallite size, crystallinity, strain, and crystal defects.

2.2.4.1 Principle of X-ray Diffraction:

X-rays constitute a form of electromagnetic radiation and characterized by significantly shorter wavelengths, typically falling within the range of 0.5-2.5 Å.

The interaction of X-rays with matter primarily occurs through engagement with electrons, involving two main processes: scattering and true absorption. When X-rays encounter a material, they scatter in various directions due to the electron cloud surrounding atoms. If the X-ray wavelength is comparable to the separation between atoms, interference may occur. X-ray diffraction peaks arise from constructive interference of monochromatic light scattered by each set of lattice planes at specific angles, with peak intensities determined by the atomic arrangement in the lattice planes. Interference maxima and minima can occur in ordered arrays of scattering centers, like atoms or ions in a crystalline solid.

In this investigation, sample analyses were carried out using a Rigaku Ultima IV X-ray diffractometer operating at 40 mA and 40 kV, utilizing a CuKα1 radiation source with a wavelength (λ) of 1.5405 Å. Data was collected in the 2θ range from 0° to 80° with a step size of 0.02. The resulting patterns were compared with JCPDS reference data for phase identification. The Scherrer equation (2.3) was applied to compute the crystallite size of the prepared samples is given as:

$$\mathrm{d} = \frac{0.89\lambda}{\beta\cos\theta} \tag{2.3}$$

Where d, λ, θ, and β are the crystallite size, X-ray wavelength (1.518 Å), Bragg diffraction angle, and full width at the half maximum (FWHM) of the diffraction peak, respectively.

2.2.5 UV-Vis Diffuse Reflectance spectroscopy (DRS) [7], [8]

The DRS analysis is a valuable method for assessing the optical properties of various materials. In DRS, the ratio of light scattered from a sample layer (thicker than 2-3 mm) to that from an ideal non absorbing reference sample is measured across different wavelengths. This technique has been widely applied in examining titania-based materials and transition metal oxides. It provides insights into surface coordination and the diverse oxidation states of metal ions by capturing information on d-d, f-d transitions, and oxygen-metal ion charge transfer bands. From DRS data, direct/indirect bandgap energy (Eg) of the material can also be calculated using the Kubelka-Munk method equation (2.4).

$$F(\mathrm{R\alpha}) = \frac{(1 - \mathrm{R\alpha})^2}{2 \times \mathrm{R\alpha}} \tag{2.4}$$

Where $F(R\alpha)$ is the Kubelka-Munk function, $R\alpha = 10^{-A}$ is the reflectance coefficient, which can be calculated from absorbance (A).

In this method, the bandgap energy (Eg) is determined by plotting $[F(R\alpha)h\nu]^{1/2}$ versus the photon energy ($h\nu$) [9] Here, the Ultraviolet-Visible (UV-Vis) absorption spectra of the synthesized photocatalysts were measured in the range of 200-800 nm by DRS analysis (CORY 100 Bio UV spectrophotometer) using barium sulfate as internal standard.

2.3 Experimental set-up:

2.3.1 Photochemical reactor for the degradation of dye:

A UV photochemical reactor (Figure 2.1) equipped with eight ultraviolet tubes of 8 watts (wavelength 2537 nm) was used for photodegradation of dye. A quartz tube for the photochemical reactor was purchased from Perfit India Ltd., Ambala (India). The dye solution was kept in the photochemical reactor's quartz tube, containing a stirring mechanism.

The MB dye was photodegraded at five distinct concentrations (10, 20, 30, 40, and 50 ppm) in aqueous solution using all the synthesized photocatalysts.

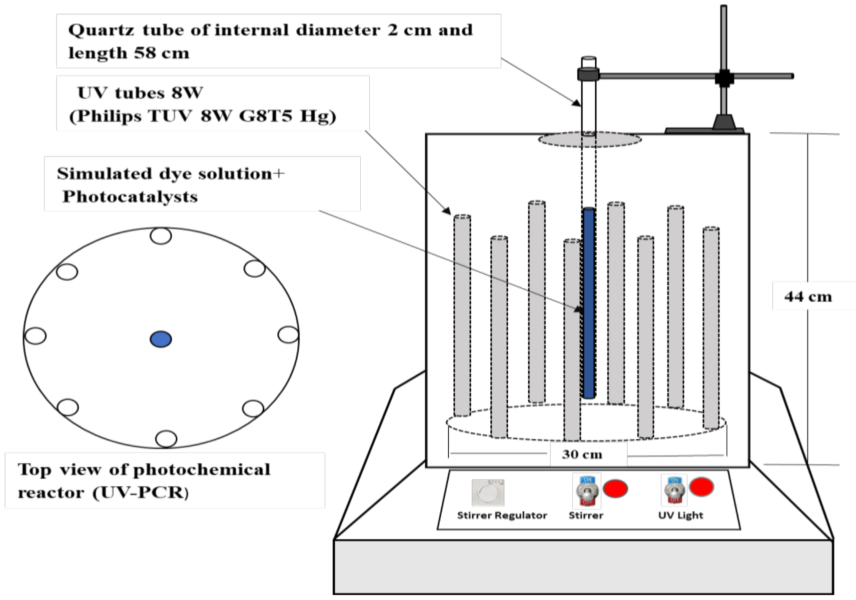

Figure 2.1 Schematic of Photochemical Reactor

2.3.2 Determination of dye concentration

The dye concentration in the unknown sample was determined using the calibration curve. This curve was generated by plotting the absorbance against concentration data for solutions of known concentrations at 663 nm.

2.3.3 Photodegradation of Methylene Blue dye

2.3.3.1 Adsorption and self-degradation study of dye

The dye might undergo degradation when exposed to UV light without any photocatalysts and attach to the surface of photocatalysts. To evaluate the impact of these two factors on dye degradation, two distinct investigations were conducted as outlined below:

2.3.3.2 Adsorption study of the dye on the photocatalysts

To assess the adsorption of the dye onto the prepared photocatalysts, a quartz tube in the reactor was filled with 100 mL of a 50 ppm dye solution. Subsequently, 0.01 g of photocatalyst was added into the solution. The tube was covered with a black paper sheet and placed in the UV-PCR for 1 h with continuous stirring, during which the UV light was not turned on. Samples of 2 mL were extracted from the tube every 10 min, and after centrifuging the contents, the colour concentration was analyzed in this study, as shown in Figure 2.2.

2.3.3.3 Self-degradation of dye (without photocatalysts)

To determine the dye's potential for self-degradation without photocatalyst, 100 mL of the dye solution was taken in the quartz tube and subjected to UV light for 3 h. A 2 mL solution was analyzed for 10 min for the photolysis process.

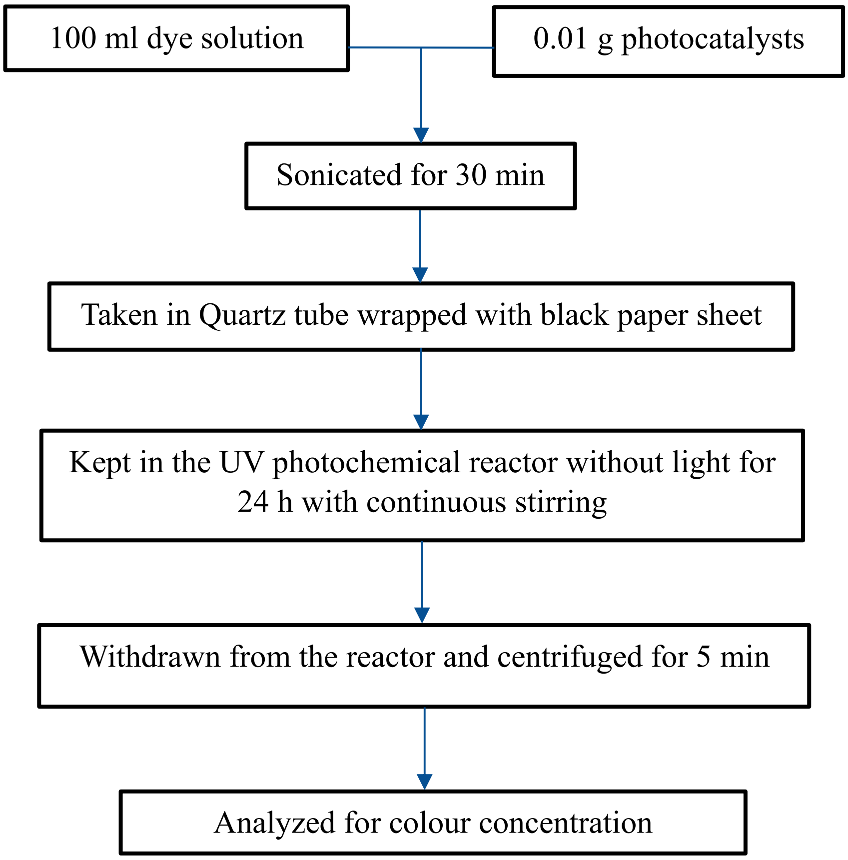

Figure 2.2 Adsorption study of dye on the synthesized photocatalysts

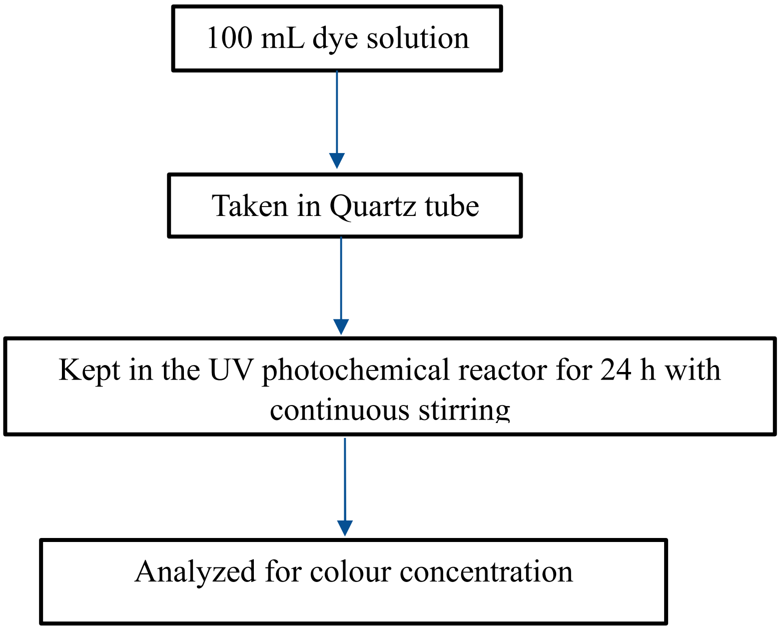

Figure 2.3 Self-degradation study of the dye in UV-PCR.

2.3.4 Kinetic study of dye degradation:

The degradation kinetics was investigated using a quartz tube in the photochemical reactor with all prepared photocatalysts. Five different aqueous dye solution concentrations were used in the experiments (10, 20, 30, 40 and 50 ppm). This quartz tube contained 100 mL of dye solution and photocatalysts. The stirrer and UV lamp were turned on. 2 mL samples were taken out at 5 min intervals for 1 h, and their dye concentration was assessed after the centrifugation of samples.

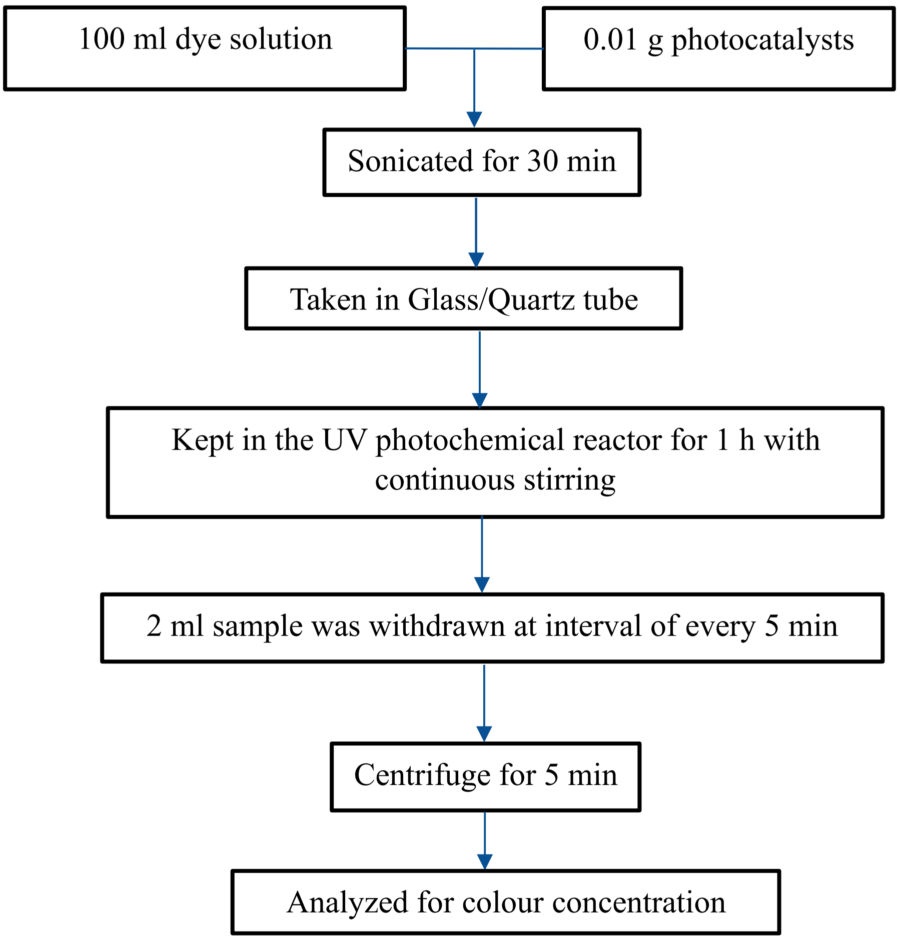

Figure 2.4 Kinetic study of dye degradation with synthesized photocatalysts

2.3.5 Photocatalytic activity of regenerated photocatalysts

The regeneration process followed the steps outlined in Figure 2.5 After the photodegradation experiments involving the degraded dye solution and the photocatalyst, the entire content was centrifuged at 3500 RPM for 20 min. This process effectively separated the used photocatalyst, settling at the bottom from the clear liquid on top. The liquid portion was extracted using a syringe, while the bottom solid, containing the used photocatalyst, underwent two washes with double distilled water (DDW) in a centrifuge at 3500 RPM for 20 min. The resulting material was placed in a glass Petri dish and dried in a dryer at 102°C. After drying, the material was ground using a pestle-mortar, transferred to a crucible, and subjected to calcination at 500°C for 5 h to obtain the regenerated photocatalyst.

Only the regeneration of 1.5% La-doped TiO_2, 3% I-doped, and 2% La & 3% I co-doped TiO_2 photocatalyst was done as per the procedure discussed as above since these showed the best photocatalytic activity (the maximum dye degradation rate) among all the synthesized photocatalysts in La-doped, I doped and La-I co-doped TiO_2 photocatalysts respectively.

2.3.6 Kinetic study with regenerated photocatalysts:

The same procedure as discussed in section 2.3.4 was used for kinetic study of degradation of MB dye with regenerated photocatalyst.

2.3.7 Calculation of dye removal/reduction

To determine the actual dye reduction caused by photodegradation by the undoped, doped, and co-doped photocatalysts, the total dye reduction was subtracted from the dye reduction caused by adsorption and the dye loss in the blank dye solution. UV-Vis spectrophotometry was used to determine the dye concentration at a wavelength of 663 nm. MB dye's photo catalytically degradation was determined by equation (2.5):

Change of concentration by photodegradation = $(C_1 - C_2) - C_3 - C_4$ (2.5)

In equation (2.5), C_1 and C_2 are the initial and final dye solution concentrations, respectively. C_3 and C_4 indicate the concentration change resulting from the self-reduction of dye and adsorption in the final solution.

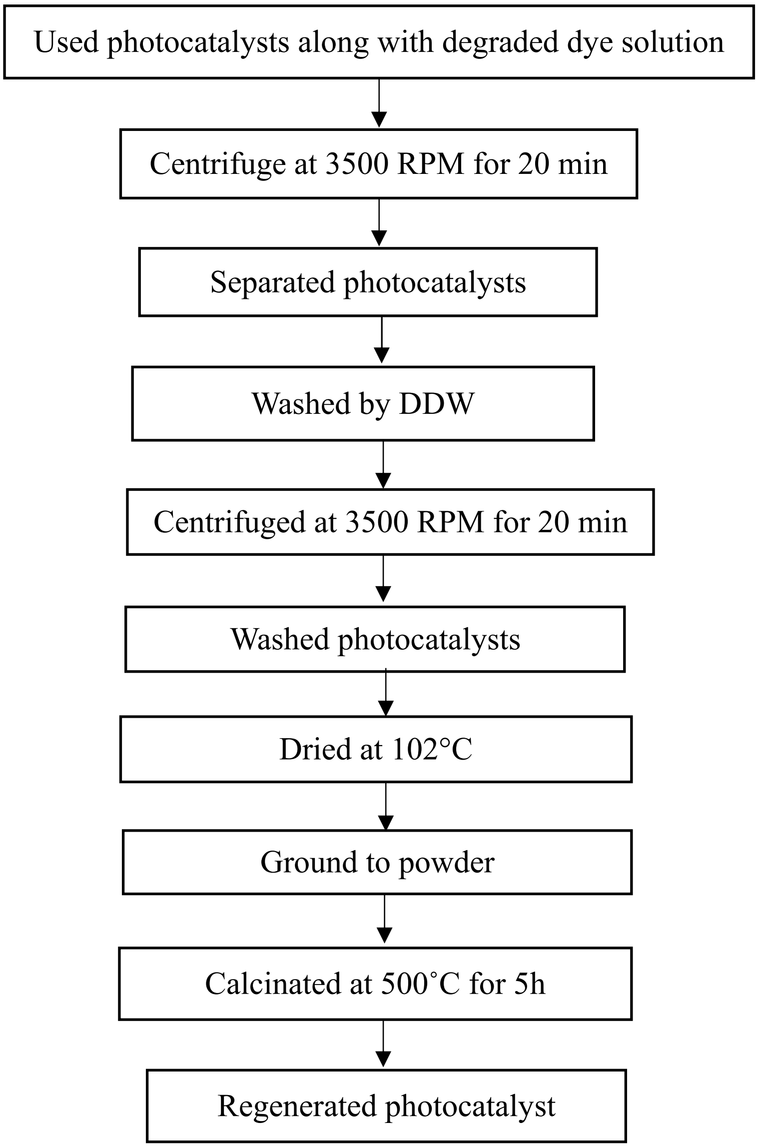

Figure 2.5 Regeneration process of TiO_2 photocatalysts.

2.3.8 Comparative study for the best photocatalysts

Three comparative studies were done to determine the best photocatalysts in each case (La doped, I doped and La-I co-doped TiO_2). The first study compared undoped TiO_2, best La-doped (1.5%) photocatalysts, and P-25. In the second study, undoped TiO_2, best I-doped (3%) photocatalysts, and Aeroxide P-25 were compared, and in the third study, undoped TiO_2, best co-doped (2% La & 3% I) TiO_2 and Aeroxide P-25 were compared. In all comparative studies, the activity of photocatalysts was examined with respect to dye degradation. From the same data overall, best catalyst was determined

2.3.9 Phytotoxicological evaluation of residual MB solution after photodegradation using *Vigna radiata* [10]:

To understand the suitability of the photocatalyst-treated MB solution for irrigation, the germination test on *Vigna radiata* seeds was done with treated dye water, distilled water, and untreated dye sample, which gives an idea about the wastewater's reusability prospects. These seeds were bought from the local market, soaked with 1% NaClO for 5 min, and rinsed several times to ensure no contaminants were present. In three Petri dishes, a 5 mm layer of cotton was covered by Whatman filter paper. At the top of it, ten seeds were also covered by Whatman filter paper. Each seed was given 5 mL of distilled water, treated water, and untreated water, and it received 10 mL of MB solution (before and after degradation) irrigation at regular intervals of 12 h. The plates were put at 30°C to germinate, and a seed was considered to have grown if the radicle length was greater than 2 mm. After 2 days, % germination was calculated, and after 5 days, % relative root growth (% RG), % relative seed germination (% SG), % phytotoxicity index (PIN), and % germination index (% GIN) were calculated.

$$\% \ \mathrm{RG} = \frac{\boldsymbol{root\ length\ of\ sample}}{\boldsymbol{root\ length\ of\ control\ sample}} \times 100 \tag{2.6}$$

$$\% \ \mathrm{SG} = \frac{germination\ of\ seed\ in\ sample}{germination\ of\ seed\ in\ control\ sample} \times 100 \tag{2.7}$$

$$\mathrm{PIN} = 1 - \frac{root\ lenth\ of\ sample}{root\ lenth\ of\ control\ sample} \times 100 \tag{2.8}$$

$$\% \ \mathrm{GIN} = \frac{RG\ \times\ SG}{100} \tag{2.9}$$

References

[1] A. Knop-Gericke, "X-ray Photoelectron Spectroscopy. An Introduction to Principles and Practices. By Paul van der Heide.," *Angew. Chemie Int. Ed.*, vol. 51, no. 37, pp. 9218–9218, 2012, doi: 10.1002/anie.201205395

[2] J. Holmes, "Photoelectron spectroscopy," *Encycl. Spectrosc. Spectrom.*, no. January, pp. 618–618, 2016, doi: 10.1016/B978-0-12-803224-4.00355-1

[3] M. Von Ardenne, P. Hawkes, and T. Mulvey, "Chapter Two - On the history of scanning electron microscopy, of the electron microprobe, and of early contributions to transmission electron microscopy☆☆Part of this article is a translation of an earlier historical article by the author, published in Optik 50, 177 (1978). Permission to publish this English version has been granted by Dr. E. Menzel and the Wissenschaftliche Verlagsgesellschaft, Stuttgart, and is gratefully acknowledged.," in *The Beginnings of Electron Microscopy - Part 1*, vol. 220, P. W. Hawkes and M. B. T.-A. in I. and E. P. Hÿtch, Eds., Elsevier, 2021, pp. 25–50. doi: https://doi.org/10.1016/bs.aiep.2021.08.002

[4] A. Khursheed, "Scanning electron microscopy," T. B. T.-E. of C. M. P. (Second E. Chakraborty, Ed., Oxford: Academic Press, 2024, pp. 36–50. doi: https://doi.org/10.1016/B978-0-323-90800-9.00128-1

[5] S. J. Pennycook, "Microscopy: Transmission electron microscopy," T. B. T.-E. of C. M. P. (Second E. Chakraborty, Ed., Oxford: Academic Press, 2024, pp. 63–70. doi: https://doi.org/10.1016/B978-0-323-90800-9.00194-3.

[6] J. Liu and J. M. Cowley, "High-resolution scanning transmission electron microscopy," *Ultramicroscopy*, vol. 52, no. 3, pp. 335–346, 1993, doi: https://doi.org/10.1016/0304-3991(93)90044-X.

[7] S. Saroj, L. Singh, and S. V. Singh, "Solution-combustion synthesis of anion (iodine) doped TiO_2 nanoparticles for photocatalytic degradation of Direct Blue 199 dye and regeneration of used photocatalyst," *J. Photochem. Photobiol. A Chem.*, vol. 396, no. April, p. 112532, 2020, doi: 10.1016/j.jphotochem.2020.112532.

[8] S. Saroj, L. Singh, and S. V. Singh, "Photodegradation of Direct Blue-199 in carpet

industry wastewater using iron-doped TiO_2 nanoparticles and regenerated photocatalyst," *Int. J. Chem. Kinet.*, vol. 51, no. 3, pp. 189–205, 2019, doi: 10.1002/kin.21243

[9] W. A. A. Mohamed et al., “Study of phytotoxicity, remarkable photocatalytic activity, recycling process and energy consumption cost of TiO_2 quantum dots photocatalyst for photodegradation of Coomassie brilliant blue R dye,” Opt. Mater. (Amst)., vol. 137, no. February, p. 113607, 2023, doi: 10.1016/j.optmat.2023.113607

[10] V. Verma and S. V. Singh, “Journal of Environmental Chemical Engineering Augmentation of photocatalytic degradation of methylene blue dye using lanthanum and iodine Co-doped TiO_2 nanoparticles , their regeneration and reuse ; and preliminary phytotoxicity studies for potential use,” J. Environ. Chem. Eng., vol. 11, no. 6, p. 111339, 2023, doi: 10.1016/j.jece.2023.111339